

## Three-dimensional coherent X-ray diffraction imaging of a ceramic nanofoam: determination of structural deformation mechanisms

A. Barty,<sup>1</sup> S. Marchesini,<sup>1,2,3</sup> H. N. Chapman,<sup>1,3</sup> C. Cui,<sup>2</sup> M. R. Howells,<sup>2</sup> D.A. Shapiro,<sup>2</sup> A. M. Minor,<sup>2</sup> J. C. H. Spence,<sup>4</sup> U. Weierstall,<sup>4</sup> J. Ilavsky,<sup>5</sup> A. Noy,<sup>1</sup> S. P. Hau-Riege,<sup>1</sup> A. B. Artyukhin,<sup>1</sup> T. Baumann,<sup>1</sup> T. Willey,<sup>1</sup> J. Stolken,<sup>1</sup> T. van Buuren,<sup>1</sup> and J. H. Kinney<sup>1</sup>

<sup>1</sup>*Lawrence Livermore National Laboratory, 7000 East Ave., Livermore, CA 94550, USA*

<sup>2</sup>*Lawrence Berkeley National Laboratory, 1 Cyclotron rd. Berkeley, CA 94720, USA*

<sup>3</sup>*Center for Biophotonics Science and Technology, University of California, Davis, 2700 Stockton Blvd., Ste 1400, Sacramento, CA 95817, USA\**

<sup>4</sup>*Department of Physics and Astronomy, Arizona State University, Tempe, AZ 85287-1504, USA*

<sup>5</sup>*Advanced Photon Source, Argonne National Laboratory, Argonne, IL, USA*

(Dated: October 22, 2018)

Ultra-low density polymers, metals, and ceramic nanofoams are valued for their high strength-to-weight ratio, high surface area and insulating properties ascribed to their structural geometry. We obtain the labyrinthine internal structure of a tantalum oxide nanofoam by X-ray diffractive imaging. Finite element analysis from the structure reveals mechanical properties consistent with bulk samples and with a diffusion limited cluster aggregation model, while excess mass on the nodes discounts the dangling fragments hypothesis of percolation theory.

The topology, fractal index, stability and structure of foams have fascinated scientists and mathematicians for decades. Foams arise in fields as diverse as cosmology (in Hawking’s theory), geology, surfactants, phospholipids, cells, bone structure, polymers and structural materials wherever lightness and strength are needed. Especially important are applications of periodic foam network theory to predictions of the structure of mesoporous crystalline materials suitable for use as catalysts [1] for cleaner fuels, and the study of the diffusion of water and oil in porous rocks. Here the rate-limiting step for diffusion is limited by the smallest pore, normally too small to be observed internally by any conventional tomographic microscopy. Aerogels are an important example of such a class of material. Described variously as “frozen smoke” and “San Francisco fog”, these terms do not refer to a particular substance itself but rather to a structural geometry a substance can assume. Many aerogels, for example, demonstrate astonishing mechanical, thermal, catalytic and optical properties, which are ascribed to their low density and porous structure[2]. However to date there have been few if any methods developed for “seeing inside” these foams in order to make an experimental determination of topology and structure at the mesoscopic length scale.

Although electron microscopy has provided the crystallinity and morphology of individual beam elements comprising the foam, no existing technique has been able to capture the three-dimensional bulk lattice arrangement over micron-scale sample dimensions. X-rays provide the penetration, lacking to electrons, which allow us to study three-dimensional structure over thicknesses of

micrometres. Current state-of-the art zone plate microscopes achieve a transverse spatial resolution of  $\approx 15$  nm half pitch (30 nm period) [3], but have difficulty sustaining this resolution through the bulk structure of micron-sized three dimensional objects due to depth of focus limitations.

We report here a three-dimensional structure determination at the mesoporous length scale ( $\approx 15$  nm) of a micron-sized fragment of aerogel obtained by inversion of coherent x-ray diffraction patterns [4]. The complexity of the structure observed is far greater than that of samples previously studied by this technique, and was made possible by advances in computational phase retrieval methods, the addition of holographic reference points near the specimen, and by the inherent sparsity of the foam. More generally, we demonstrate the ability of diffraction imaging to image an unknown, isolated object at high resolution in three dimensions, opening the door to a wide range of applications in material science, nanotechnology and cellular biology.

The aerogel sample imaged here is a low density (100 mg/cc, 1.2% bulk density) high-Z  $\text{Ta}_2\text{O}_5$  metal oxide nanofoam, chosen because of its potential use in double shell laser ignition targets for fusion (which require a very low density material with high Z) and because of its stability under an intense x-ray beam. Because the strength of these ultra-low density foams is orders of magnitude less than expected, it is important to understand and identify the unique microstructures of these foams, and to relate them to the bulk physical properties. Using the structure observed as a high-fidelity template for finite-element analysis we calculate the load displacement response of the foam, and compare the resulting stiffness against various structural models.

X-ray diffraction imaging is elegant in its experimental simplicity: a monochromatic and coherent X-ray beam illuminates the sample, and the far-field diffraction pat-

\*Correspondence and requests for materials should be addressed to S. Marchesini:smarchesini@lbl.gov

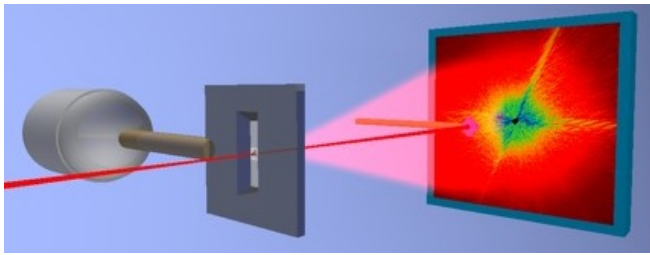


FIG. 1: Diffraction imaging layout. Coherent X-rays ( $\lambda = 1.65$  nm) illuminate [5, 6] the sample mounted on a 50 nm thick  $\text{Si}_2\text{N}_3$  membrane window. Diffraction patterns at various sample orientations ( $+69^\circ$  to  $-64^\circ$  in  $1 \pm 0.1^\circ$  increments) are measured using a CCD camera (20  $\mu\text{m}$  pixel size,  $1300 \times 1340$  pixels, 165 mm downstream). A beamstop blocks the direct beam and multiple exposure times are summed to expand the CCD dynamic range.

tern from the object is recorded on an area detector (Figure 1). Multiple orientations fill out a three-dimensional diffraction volume, which is proportional to the Fourier transform of the object index of refraction. The detection system records only the diffracted intensities, but phase retrieval techniques can be applied to recover a three-dimensional image of the sample [7, 8, 9]. The feasibility of this technique for reconstructing an image of the sample from its diffraction pattern has been well demonstrated in many X-ray diffraction experiments [4, 11, 13, 14, 15].

A 3D implementation of the HIO algorithm [7] was used for phase reconstruction on the 3D volume with feedback parameter  $\beta = 0.9$  and support refinement [10] for 1200 iterations, followed by the RAAR algorithm [8] through to iteration 3000 also with feedback parameter of  $\beta = 0.9$ . Missing data from both the central beamstop and inaccessible sample rotations was accounted for during phase retrieval using the *Shrinkwrap* algorithm, in which the object support itself acts as a constraint in the regions of missing data [10, 14]. By applying full three dimensional phase retrieval directly to the 3D diffraction volume, as done here, we avoid the inconsistencies and image alignment problems caused by dividing the phase retrieval and tomographic data assembly into two separate steps performed sequentially [11]. Ewald sphere curvature included in the 3D data assembly avoids defocus artifacts typical of such two step reconstruction process, as well as any lens-based micro-tomography volume reconstruction. The phase reconstruction techniques employed here, including a detailed analysis of spatial resolution and methods for handling the limited number of views, missing angles and central beamstop are described in detail elsewhere [14] (see also supplemental material[12]).

The aerogel itself was prepared by a sol-gel process that involved the controlled hydrolysis of tantalum ethoxide, followed by rapid supercritical extraction of the reaction solvent [16]. The tantala aerogels obtained from this particular formulation are isolated as translucent monoliths

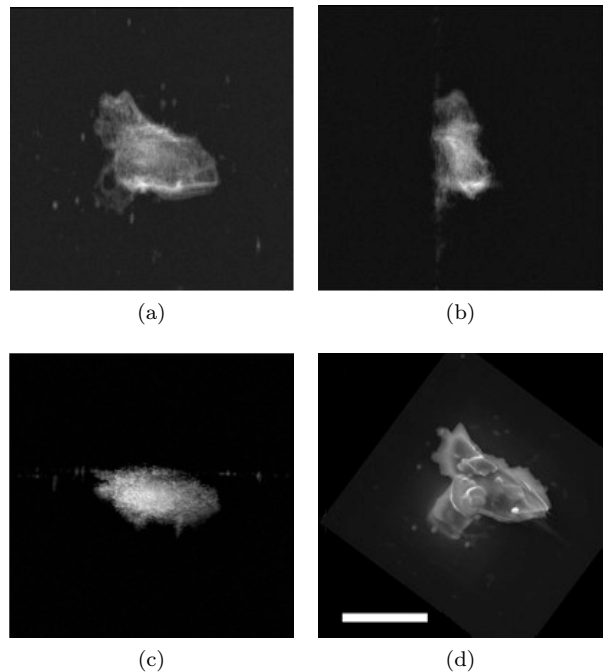


FIG. 2: (a-c) Orthogonal projections through the amplitude of the reconstructed 3D object. The imaged volume is 5  $\mu\text{m}$  cubed with a reconstruction resolution of 15 nm. A top-down SEM image of the prepared aerogel sample for comparison with the 3D reconstruction is shown in panel (d), scale corresponds to 2  $\mu\text{m}$ . Several reference platinum dots (d) are reconstructed on the membrane plane (b, c) and the animation in supplementary materials[12].

with bulk densities of approximately 100 mg/cc, as determined from bulk sample mass and dimensions. We mounted an irregular 1-2  $\mu\text{m}$  sized piece on a 50 nm thick rectangular silicon nitride membrane window of 2 mm x 50  $\mu\text{m}$  size supported in a 200  $\mu\text{m}$  thick silicon wafer frame. Several 50 nm platinum dots were placed in proximity to the sample using an electron beam to locally decompose a metal-organic precursor gas (Figure 2). These dots diffract reference waves that provide holographic information and act as heavy atoms in the phase retrieval process, and additionally provide known structures on the Silicon membrane for verification of reconstruction fidelity and spatial resolution (Figure 3). High resolution structural information is required to fully characterize mechanical properties of these aerogels, however many other statistical properties such as density and correlation distances can be obtained directly by standard analysis of the radially averaged small angle x-ray scattering (SAXS) patterns. We note however that the radially averaged raw diffraction data used in our reconstruction has a power law exponent of about -4, while diffraction patterns generated by a reconstructed 3D region containing only aerogel material reveals a power law exponent of -2 (Fig. 4), typical of the “string of pearls” aerogel morphology (see below). This is because our measured

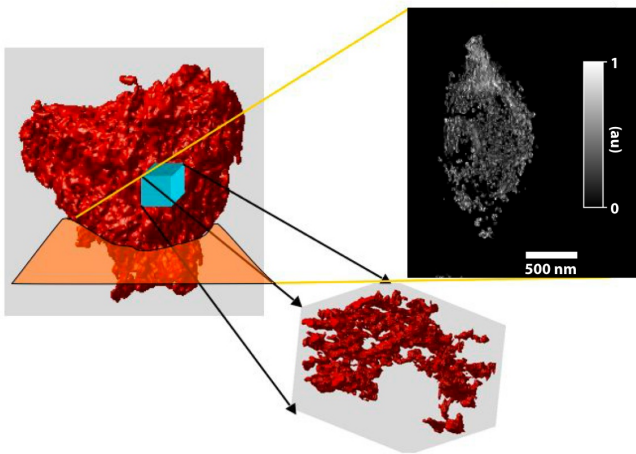


FIG. 3: Section and isosurface rendering of a 500 nm cube from the interior of the 3D volume. The foam structure shows globular nodes that are interconnected by thin beam-like struts. Approximately 85 % of the total mass is associated with the nodes, and there is no evidence of a significant fraction of dangling fragments.

data contains additional scattering from the membrane, surrounding particles and Pt contamination. These scatterers are physically separated in the 3D reconstruction, enabling scattering from just the aerogel portion of the sample to be calculated.

X-ray scattering measurements extending the spatial scales probed by diffractive imaging data were performed on a similar batch of aerogel foam at beamline 33-ID at the Advanced Photon Source (APS) [24, 25]. Three distinct power-law regimes are observed at different spatial scales (Fig. 4). In the Porod region below  $q \simeq 0.1 \text{ \AA}^{-1}$  a power law with an exponent of -4 indicates that the foam has a smooth surface. The form factor region from  $q \simeq 0.1 \text{ \AA}^{-1}$  to  $q \simeq 0.005 \text{ \AA}^{-1}$  provides information on the shape of the individual scattering elements in the aerogel network. In this region we have a power law exponent of -2, which describes a mass fractal of dimension 2 which is consistent with a diffusion limited cluster aggregation or the typical “string of pearls” aerogel morphology. Oscillations in the calculated (XDM) scattering are due to the size of aerogel sub-region used to create the calculated plot. The cross over points between the changing slopes occur at  $q_1 \simeq 0.1 \text{ \AA}^{-1}$  and  $q_2 \simeq 0.09 \text{ \AA}^{-1}$  with an associated radii of gyration of  $Rg_1 \simeq 20 \text{ \AA}$  and  $Rg_2 \simeq 140 \text{ \AA}$  respectively. Values of the power law exponents and radii of gyration are obtained by standard Porod and Guinier analysis. For aerogels a fractal analysis is commonly used to interpret the scattering data. In the fractal model  $Rg_1$  and  $Rg_2$  are related to the mean particle diameter and the correlation range, where the relation between  $Rg$  and size or correlation range depends strongly on the shapes and size distribution of the scatters. At very low  $q$  we find another power law slope associated with another scattering feature, however the USAXS data end before a clear radius of gyration is observed therefore it is not possible

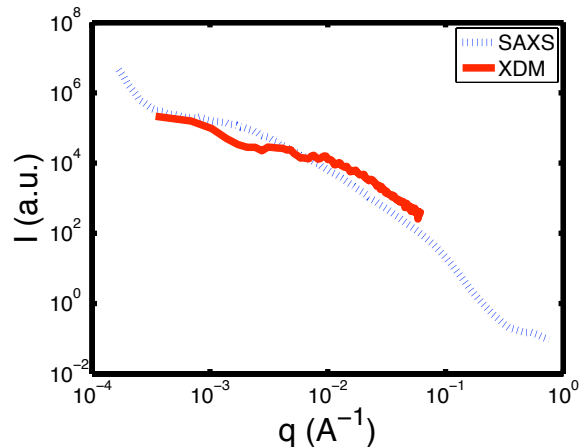


FIG. 4: Small angle X-ray scattering data calculated from our 3D volume reconstruction (XDM) compared to ultra small angle X-ray scattering (SAXS) measurements on a similar batch of 100 mg/cc  $\text{Ta}_2\text{O}_5$  aerogel.

to estimate the size of these structures. We can, however, limit the size of these features to more than 1 micron, the size related to the minimum scattering vector at which we still observe the power law slope behavior. Voids of several hundred nanometers are observed in the reconstructed 3D volume.

We now turn our attention to understanding the mechanical properties of these aerogels. The strength and stiffness of three-dimensional foams are often observed to scale as  $\rho_a^m$ , where  $\rho_a$  is the density of a structure divided by the density of its constituent members. In a model proposed by Gibson and Ashby [17] the scaling exponent  $m$ , has limiting values of 1 where deformation is axial, and 2 for structures that deform in bending. Scaling relations in terms of  $\rho_a$  assume some degree of uniformity in the distribution of mass between the interconnecting lattice “beams” and the nodes that define their intersections. These assumptions appear satisfied for many foam-like structures at densities down to 10% or less ( $\rho_a \lesssim 0.1$ ). However the strength of many low density aerogel samples of much lower density (densities of less than 1% or  $\rho_a \ll 1$ ) is orders of magnitude less than expected and scaling exponents between 3 and 4 are frequently observed [18, 19]. Higher mass scaling exponents are attributed to the presence [20] of fragments disconnected from the load-bearing backbone structure [19], adding mass without carrying or transferring load. These disconnected fragments are a natural consequence of percolation: as a structure approaches a critical density, more of its mass becomes associated with branches disconnected from the backbone of the lattice.

It is not clear, however, that such percolation models apply to these aerogels [20, 22]. In one alternative model, heterogeneities such as micron-sized holes produce spanning structures that could fail by buckling [22]. Yet another model proposes that diffusion-limited clus-

ter aggregation leads to fractal clusters (blobs) connected by thin beams (links) [20, 21]. The response of the “blob and link” architecture to compressive loading is simulated with finite-element modeling, using the NIKE3D implicit finite-element solver [23]. Material data for polycrystalline tantalum oxide was used for the constitutive model with the modulus being 140 GPa. For these simulations, opposing faces are loaded in compression, while the unloaded cube faces are treated with mirror symmetry, restricting boundary motion to the plane. The average mass scaling exponent obtained by this modelling was  $m = 3.6$ , consistent with bulk data. When the excess node mass was removed by computational thinning, the scaling exponent reverted to  $m = 2$ , indicating that the primary deformation mechanism was bending of the interconnecting struts.

In this first experimental high-resolution view inside a foam, we see a structure consisting of nodes connected by thin beams. These are similar to the simulated fractal cluster aggregates and links derived from a diffusion-limited cluster aggregation model. This blob and beam structure explains why these low density materials are weaker than predicted, and explains the high mass scaling exponent observed for this material. Computational thinning of the measured structure improves the strength-to-weight ratio by orders of magnitudes, indicating that improvements in the strength could be obtained by modifying the aerogel preparation conditions in an effort to redistribute constituent material from nodes to interconnected struts. Improvements in resolution using brighter light sources, shorter wavelengths and larger detectors would enable resolving the cross section of in-

terconnecting struts, providing a full characterization of not only these aerogels but also a range of engineered nanoscale materials. The structural analysis we demonstrated here could be applied to other porous materials and assist modelling percolation problems such as oil and water in minerals[29, 30]. More generally the ability to image an unknown, isolated object in three dimensions at high resolution, as demonstrated here, has the potential for a wide range of applications in material science, nanotechnology and biology at the cellular level.

### Acknowledgments

This work was supported by The U.S. Department of Energy under Contract W-7405-Eng-48 to the University of California, Lawrence Livermore National Laboratory; Projects 05-SI-003 and 05-ERD-003 from the Laboratory Directed Research and Development Program of LLNL; the Advanced Light Source and the National Center for Electron Microscopy, Lawrence Berkeley Lab, under DOE Contract DE-AC02-05CH11231. JCHS and UW supported by DOE grant DE-FG03-02ER45996. The National Science Foundation through the Center for Biophotonics, UC Davis, under Cooperative Agreement No. PHY0120999. Use of the Advanced Photon Source was supported by the U.S. Department of Energy, Office of Science, Office of Basic Energy Sciences, under Contract No.W-31-109-ENG-38. The authors have no competing financial interests.

- 
- [1] S. Bag et al. *Science* 317, 490 - 493 (2007)
  - [2] L. W. Hrubesh, *Journal of Non-Crystalline Solids* 225, 335-342 (1998).
  - [3] W.L. Chao, et al. *Nature* 435, 1210-1213 (2005).
  - [4] J. Miao, P. Charalambous, J. Kirz & D. Sayre, *Nature* 400, 342-344 (1999).
  - [5] M.R. Howells et al. *Journal de Physique IV* 104, 557-561 (2003).
  - [6] T. Beetz, et al. *Nuc. Instr. & Meth. Phys. Res. A* 545, 459-468 (2005).
  - [7] J. R. Fienup, *Appl. Opt.* 21, 2758-2769 (1982).
  - [8] D.R. Luke, *Inverse Problems* 21, 37-50 (2005).
  - [9] S. Marchesini, *Rev. Sci. Inst.* 78, 011301 (2007).
  - [10] S. Marchesini et al. *Phys. Rev. B* 68, 140101(R) (2003).
  - [11] J. Miao et al. *Phys. Rev. Lett.* 97, 215503 (2006).
  - [12] See EPAPS Document No. [] for details on the methods. For more information on EPAPS, see [ftp://ftp.aip.org/epaps/phys\\_rev\\_lett/](ftp://ftp.aip.org/epaps/phys_rev_lett/) [Document No.].
  - [13] D. Shapiro et al. *Proc. Nat. Acc. Sci.* 102, 15343-15346 (2005).
  - [14] H. N. Chapman et al. *J. Opt. Soc. Am. A* 23, 1179-1200 (2006).
  - [15] M.A. Pfeifer, G.J. Williams, I. A. Vartanyants, R. Harder, & I. K. Robinson, *Nature* 442, 63-66 (2006).
  - [16] C.J. Brinker & W. S. George, *Sol-Gel Science: The Physics and Chemistry of Sol-Gel Processing*. (Academic Press, 1990).
  - [17] L.J. Gibson & M. Ashby, *Cellular Solids: Structure and Properties, Edn. 2nd.* (Cambridge University Press, 1997).
  - [18] H.S. Ma, A.P. Roberts, J. H. Prevost, R. Jullien, & G. W. Scherer, *Jour. of Non-Crystalline Solids* 277, 127-141 (2000).
  - [19] R.W. Pekala, L. W. Hrubesh, T. M. Tillotson, C. T. Alviso, J. F. Poco, J. D. LeMay, in *Mechanical properties of porous and cellular materials*, Vol. 207, 197 (Materials Research Society, Boston, MA; 1990).
  - [20] H.S. Ma, J. H. Prevost, R. Jullien, & G. W. Scherer, *Journal of Non-Crystalline Solids* 285, 216-221 (2001).
  - [21] P. Meakin, *Phys. Rev. Lett.* 51, 1119-23, (1983).
  - [22] R. Pirard & J. P. Pirard, *Journal of Non-Crystalline Solids* 212, 262-267 (1997).
  - [23] B.N. Maker, R.M. Ferencz, & J. O. Hallquist, NIKE3D, A Nonlinear, Implicit, Three-Dimensional Finite Element Code For Solid And Structural Mechanics 1995. LLNL report UCRL-MA-105268
  - [24] J. Ilavsky, A. J. Allen, G. G. Long, P. R. Jemian, *Rev. Sci. Instrum.* 73, 1660 (2002).

- [25] J. Ilavsky, P. R. Jemian, A. J. Allen, G. G. Long, AIP Conf. Proc. **705**, 510 (2004).
- [26] J. Ilavsky, P. R. Jemian, Irena and Indra SAXS Data Analysis Macros, <http://www.uni.aps.anl.gov/admin/sciprogram.html>
- [27] D.W. Schaefer, K.D. Keefer, Phys. Rev. Lett. **56**, 2199, (1986)
- [28] A. Hasmy, R. Vacher, R. Jullien, Phys. Rev. B **50**, 1305(1994).
- [29] D. Stauffer. "Introduction to percolation theory" (Taylor and Francis, 1985).
- [30] B. Bollobás, O. Riordan, "Percolation" (Cambridge Univ. Press, 2006).

### Supplemental online material

*Experimental equipment and methods:* The Aerogel sample was imaged at beamline 9.0.1 [5] of the Advanced Light Source (ALS), Berkeley, using the diffraction apparatus of Stony Brook University described in detail elsewhere [6]. The sample is coherently illuminated by 750eV x-rays (1.65 nm wavelength) from an undulator source using a zone plate monochromator. A 5  $\mu\text{m}$  pinhole at the zone plate focus selects a transversely coherent patch of the illuminating beam and also selects the wavelength with a spectral resolution of  $\lambda/\Delta\lambda = 1000$ . The finite spectral resolution limits image width to 1000 resolution elements in each direction [14]. The 5- $\mu\text{m}$ -diameter monochromator exit pinhole also selects a transversely spatial coherent patch of the beam.

The sample is located 20 mm downstream of this pinhole and is rotated from  $69^\circ$  to  $64^\circ$  in  $1^\circ$  increments perpendicular to the X-ray beam to obtain diffraction patterns for different projections through the object, the missing angle range corresponding to sample tilts where the beam is obscured by the slotted window. A moveable beamstop blocks the undiffracted direct beam from impinging on the CCD, as shown in Figure 1 of the main text, and is translated in separate exposures to minimize the region of missing data at low spatial frequencies. Diffraction from the sample is measured using a water-cooled Princeton Instruments PI-MTE 1300 direct detection in-vacuum CCD camera located 164mm behind the sample. The CCD chip itself is composed of a 1300x1320 array of 20  $\mu\text{m}$  pixels and is cooled to  $-45^\circ\text{C}$  to reduce dark noise. We selected sub-arrays of  $1200 \times 1200$  elements, centered on the location of the zero spatial frequency (direct beam). At these CCD and wavelength settings we have a real-space sampling interval in  $x$  and  $y$  of  $\Delta x = 11.3\text{nm}$  (in the small-angle approximation) and a field width of  $w = 13.6\mu\text{m}$ . Because the intensity across the diffraction pattern varies by orders of magnitude, multiple exposures were taken at each rotation and summed together to increase the CCD dynamic range [14].

*Phase retrieval:* For each view of the sample, the measured diffraction intensities are proportional to the modulus squared of the Fourier transform of the wave

exiting the object. However the diffraction pattern on its own contains incomplete information about the object - obtaining an image of the object requires knowledge of the optical phase of the diffraction pattern.

If the diffraction pattern intensities are sampled finely enough it is possible to solve for the diffraction pattern phases and, thus, produce an image of the object in real space [7, 10]. The feasibility of this technique for reconstructing an image of the sample from its diffraction pattern has been well demonstrated in many X-ray diffraction experiments [4, 11, 13, 14, 15].

The individual measured diffraction patterns consist of 2D CCD images, which in turn correspond to Ewald sphere sections through the 3D diffraction volume. The Ewald sphere geometry is completely defined by the known experimental geometry (pixel size, CCD distance, wavelength, sample rotation, etc.). It is therefore possible to uniquely map the locations of each pixel of each diffraction pattern into a corresponding location in the 3D diffraction volume. The transform to perform this mapping is described in detail elsewhere [14]. Here, we used a simple gridding procedure that placed individual 2D intensities in the nearest corresponding 3D voxel, although we note that more sophisticated interpolation algorithms could be applied. All other voxels in the data set were left blank, denoting regions of unknown data. This Ewald sphere mapping is performed such that the highest resolution data collected by the selected  $1200 \times 1200$  sub-arrays is fully captured in the 3D diffraction volume. Pixels where the Fourier space data was not known were allowed to be unconstrained in both Fourier space phase and magnitude during the reconstruction process. We note that Ewald sphere shells have a maximum separation of no more than 4 pixels at the edge of the diffraction volume, smaller than the observed speckle size in our data. Because the measured diffraction pattern is invariant with respect to translation of the object and reconstruction is performed directly on the three dimensional diffraction volume, there is no need to align individual 2D projections with respect to one another before reconstructing the 3D image. Instead, it is necessary to determine the centre of each diffraction pattern before assembling the 3D diffraction volume.

To obtain the real-space object structure from the diffraction volume, iterative phase retrieval was performed using a 3D implementation of the HIO algorithm [7] with feedback parameter  $\beta = 0.9$  for 1200 iterations, followed by the RAAR algorithm [8] through to iteration 3000 also with feedback parameter of  $\beta = 0.9$ . Values in the object reconstruction were allowed to be complex valued, and phase retrieval was performed based on the measured diffraction data alone. Due to both the size of the reconstruction mesh and the large number of 3D Fourier transforms required to perform iterative phase retrieval a cluster computing solution was used to process the data. Reconstructions were performed on a 16-node 2.0GHz dual processor Macintosh G5 X-serve cluster (32-CPU in total) with Infiniband interconnects and

4GB memory per node. For optimum Fourier transform speed we used the `dist_fft` distributed fast Fourier transform library from Apple Computer. volume using either 2 Fourier transforms per iteration This diffraction volume supports a field of view of  $5.8 \mu\text{m}$  with a real-space 3D reconstruction for this diffraction volume required 3000 iterations of the phase retrieval loop and took 2.5 hrs to complete. Methods for handling the missing angles and limited number of views were identical to those previously described elsewhere, and the spatial resolution of our result is necessarily band-limited by the CCD numerical aperture [14].

*Image resolution:* Critical estimation of the reconstruction resolution is important and can be performed using a variety of conventions adopted by different research groups. The spatial resolution of our imaging system is ultimately limited by the subtended numerical aperture, describing the highest spatial frequency in the object which could theoretically be imaged: finer resolution detail is simply not captured by the detector, therefore can not be physically measured. For our imaging geometry (750eV,  $20 \mu\text{m}$  pixels,  $1200 \times 1200$  pixel sub-array, and 164 mm CCD distance) we have an upper limit on spatial resolution determined by the subtended numerical aperture - namely a resolution of 11.3 nm at the edge of the CCD, decreasing to 8 nm in directions towards the corners of the CCD chip. Resolution is degraded in the longitudinal direction due to the wedge of missing data, as previously observed [14].

Achieving this resolution assumes a perfect detector, adequate measured signal out to the resolution limit, and a perfect phase retrieval algorithm. In diffraction microscopy intensities are sampled not in a focal plane of a lens but in the plane of the lens itself, therefore it is necessary to have sufficient photons measured at the claimed spatial resolution limit in order to justify any resolution claims. Crystallographers have, by convention, adopted a signal-to-noise ratio (SNR) of 3 as the threshold of resolution, measured as the SNR in a Bragg peak compared to the background noise level. The equivalent measure in diffraction microscopy of a continuous object, where there are no discrete Bragg peaks, is the SNR of the speckles relative to the background noise level. For our data, the "SNR > 3" criterion is satisfied out to the edge of the CCD camera in each individual diffraction image, where we have a mean of 18 photons/pixel signal above background levels (SNR > 4).

It is well known that sufficient angles must be measured so that the spacing between Ewald spheres in reciprocal space is less than the typical spacing between Bragg peaks in order to avoid artifacts from interpolation. In the case of continuous diffraction patterns, the angular sampling must be at least as fine as individual speckle size in the diffraction data. For our data set, the object width is  $\approx 3 \mu\text{m}$ , thus the oversampling ratio for this case is greater than 4 ( $s = 4.5$ ). With 1 degree sampling, the spacing between measured planes is at most 4 pixels at the very edge of the diffraction volume, imply-

ing that each speckle is at sampled at least once in our data. Crowther's criterion, on the other hand, dictates that the critical sampling of diffraction intensities ( $s = 2$ ) when

$$\Delta\phi = \Delta q/q_{\text{max}} = \Delta x/D. \quad (1)$$

leading to a requirement for  $0.25^\circ$  separation between planes in order to adequately sample the finest features. In practice we collect diffraction data with angular increments that are 2–4 times larger than the Crowther criterion. In the process of phase retrieval we additionally recover both the amplitudes and phases of the missing data between the Ewald surfaces, including those in a large gap resulting from a limited range (usually  $\pm 70^\circ$ ) of rotation angles, data blocked by a beam-stop, and the missing "cone" of data resulting from rotating the sample about a single axis. The quantitative effects of this procedure on image resolution was studied in detail in [14], to which we refer readers for a detailed discussion of the subject. The effect of this missing wedge of missing data corresponding to inaccessible sample rotation angles yields lower resolution in the  $z$  direction as previously observed [14].

In diffraction imaging, reconstruction algorithms and techniques perform the role typically ascribed to lenses in an imaging system. It is therefore important to assess performance of the phase retrieval process in addition to the photon detection system for stability and uniqueness of the final solution. The performance of our imaging technique could, in principle, be quantified in Fourier space by measuring the modulation transfer function (MTF) of the imaging system as a whole. For the numerical reconstruction technique used here this MTF would encapsulate resolution limits due to signal-to-noise, data alignment and regions of missing data, as well as algorithm stability and uniqueness. The phase retrieval process recovers the diffraction phases with a limited accuracy, due to factors including SNR of the diffraction amplitudes, missing data, the inconsistency of constraints, and systematic errors in the data (such as errors in interpolation). The MTF itself can be calculated only if the original object is known, and is therefore not applicable to evaluating the resolution of an unknown object. However, we can compute the stability of the phase retrieval process itself by comparing the mean reconstructed Fourier space intensities with our measured data. An equivalent MTF for phase retrieval can be determined by calculating the phase retrieval transfer function (PRTF), which represents the effective transfer function of our numerical imaging system. Details of the PRTF calculation have been previously in detail elsewhere [13, 14]. Where the phases are consistently retrieved to the same value, the squared modulus of the average will be equal to the constrained modulus, and the ratio will be unity. Where the phases are random and completely uncorrelated, the average will approach zero. Thus, the ratio is effectively a transfer function for the phase retrieval process, and the average image

is the best estimate of the image: spatial frequencies are weighted by the confidence in which their phases are known [13]. A conservative estimate of the resolution is given by the frequency at which the PRTF reaches a value of 0.5. We calculated the PRTF for our reconstruction, and it remains above a value of 0.5 right to the edge of our measured data, indicating that we indeed obtained a diffraction limited image of the sample.

Finally, we note that imaging system resolution is typically evaluated using a known object rather than an unknown object. The reasons are obvious: with a known object it is possible to quantitatively compare the initial object with the image and thereby determine the resolution of the imaging system, whereas for an unknown object there is necessarily doubt as to whether it is the object or the imaging system which is imposing limits on spatial resolution. System resolution is typically evaluated by first imaging a known object to determine system resolution, and then imaging subsequent objects under identical conditions: if the imaging process is assumed to be deterministic, the achievable resolution for the two imaging systems should be the same. We followed this standard approach by first imaging a known test object and analysing the spatial resolution in detail, then applying the same imaging methods to unknown samples. Our discussion of system resolution were presented in detail elsewhere [14], demonstrating that the imaging technique applied here faithfully reproduces a known test object up to the stated resolution limits. Here, we apply the same techniques to a new, unknown object, and once again arrive at a similar estimate of system resolution. Unlike the gold ball pyramid, the aerogel sample imaged here is of unknown structure and therefore limited use in performing a detailed analysis of system resolution.

*Finite element analysis:* For finite element analysis, a subset was taken from the interior of the reconstructed particle near the center to produce a finite box of material. The mesh was generated by assuming that any voxel partially occupied at least half-way (as determined by the voxel value) was solid material, followed by a threshold to generate the mesh. The voxel size was 8.9 nm and the cube was 94 voxels on a side. The assigned modulus and hardness were taken from the literature as 140 GPa and 5.3 GPa, respectively. The volume fraction was estimated as the number of elements (74150) divided by the volume of the cube (943), which is 0.089. Using mirror boundary conditions, the cube was compressed parallel to each of the three faces to a strain of 1stiffness is strongly dependent upon the orientation. The estimated stiffness in the X, Y, and Z directions were 25.0, 11.6, and 16.7 MPa, respectively. Based on the calculated volume fraction the exponents of the modulus vs fraction power laws for each direction are 2.62, 3.89, and 3.74, for XYZ respectively. The highest stresses were recorded in the X compressed sample was 2.3 GPa at 1% compression. The resulting stress-strain response along with the associated stiffness is plotted in Figure 4.

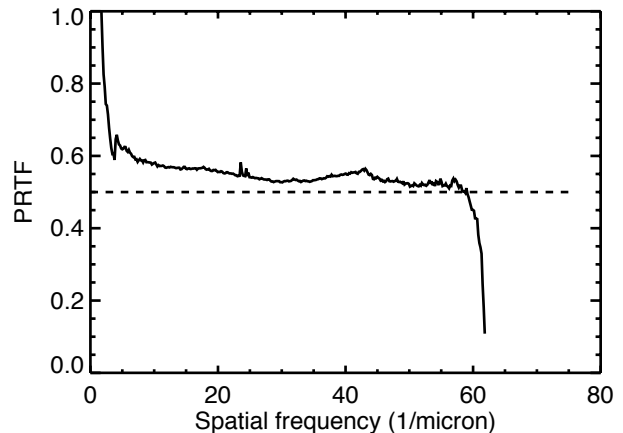


FIG. 5: Phase retrieval transfer function (PRTF) averaged over shells of constant  $u$  for the entire 3D data volume. The PRTF remains above 0.5 to the edge of measured data, indicating that our phase retrieval produces a diffraction limited reconstruction to a resolution of 11.3 nm [14], corresponding to the spatial frequency at the edge of the CCD. Indeed the PRTF remains above 0.5 out to 8 nm, which is near the diagonal corner of the CCD.

*USAXS data:* USAXS data was acquired at beamline 33-ID at the Advanced Photon Source, Argonne National Laboratory [24, 25]. The end station consists of a Bonse-Hart camera, which can measure scattering vectors ( $q$ ) from about 0.0015 to 10 nm<sup>-1</sup>. The energy of the incident x-rays in the scattering experiments was 9.7 keV below the tantalum L3 edge. Scattering data was processed using the codes developed for use on this USAXS instrument, and included absolute scattering intensity calibration and slit desmearing [26]. In the Ta<sub>2</sub>O<sub>5</sub> aerogel two distinct power-law regimes are observed with an exponent of 4 in the Porod region, and approximately -2 in the form factor region. The cross over points between the changing slopes occur at  $q_1 \approx 0.1 \text{ \AA}^{-1}$  and  $q_2 \approx 0.09 \text{ \AA}^{-1}$  with an associated radii of gyration of  $R_{g1} \approx 20 \text{ \AA}$  and  $R_{g2} \approx 140 \text{ \AA}$  respectively. Values of the power law exponents and radii of gyration are obtained by standard Porod and Guinier analysis. For aerogels a fractal analysis is commonly used to interpret the scattering data. In the fractal model  $R_{g1}$  and  $R_{g2}$  are related to the mean particle diameter and the correlation range (pore diameter or fractal size). A weakness of this analysis is that the relation between  $R_g$  and size or correlation range depends strongly on the shapes and size distribution of the scatters. If we assume roughly spherical particles  $R_{g1}$  translates into a mean diameter of 5 nm. This agrees favorably with TEM analysis of the tantalum aerogel which images particles on the order of 3-5 nm in diameter particularly given that the Guinier analysis overestimates the mean diameter in a polydispersed systems [28]. We note that the scattering data for the tantalum aerogel is similar to that measured from a silica aerogel [27].

*USAXS comparison:* Calculated SAXS data for the Aerogel foam we imaged was generated by extracting a cube of 128 voxels on a side consisting of only the Aerogel portion of the reconstructed volume. This was Fourier transformed to obtain scattering from the Aerogel structure alone, and radially averaged to obtain SAXS data corresponding to three orthogonal views through the sample. Scattering angle  $q$ -vectors were calculated from the known reconstruction voxel size, and an arbitrary scale factor was applied to the intensity for comparison

to the APS data (this shifts the plot vertically on Figure 4 but does not change the gradient on a log plot). We note that SAXS analysis performed on both the entire reconstructed volume, and on the raw diffraction data collected at beamline 9.0.1, did not agree with the APS USAXS data. We attribute this to scattering from the membrane and surrounding particles, as visible in the 3D reconstruction, and which could be avoided by extracting a sub-cube from the 3D data as described above.